

Journal of Materials Chemistry A

Accepted Manuscript



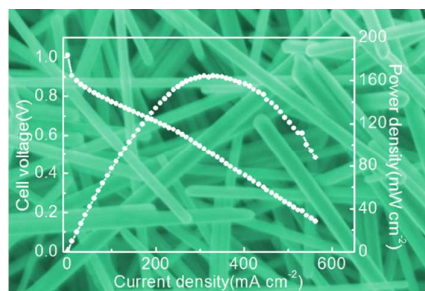
This is an *Accepted Manuscript*, which has been through the Royal Society of Chemistry peer review process and has been accepted for publication.

Accepted Manuscripts are published online shortly after acceptance, before technical editing, formatting and proof reading. Using this free service, authors can make their results available to the community, in citable form, before we publish the edited article. We will replace this *Accepted Manuscript* with the edited and formatted *Advance Article* as soon as it is available.

You can find more information about *Accepted Manuscripts* in the [Information for Authors](#).

Please note that technical editing may introduce minor changes to the text and/or graphics, which may alter content. The journal's standard [Terms & Conditions](#) and the [Ethical guidelines](#) still apply. In no event shall the Royal Society of Chemistry be held responsible for any errors or omissions in this *Accepted Manuscript* or any consequences arising from the use of any information it contains.

Graphical Abstract



The use of supportless Ag NWs enabled the H₂/O₂ AEMFC to yield a peak power density of 164 mW cm⁻².

Cite this: DOI: 10.1039/c0xx00000x

www.rsc.org/xxxxxx

ARTICLE TYPE

High-Performance Supportless Silver Nanowire Catalyst for Anion Exchange Membrane Fuel Cells

L. Zeng, T.S. Zhao*, L. An

Received (in XXX, XXX) Xth XXXXXXXXX 20XX, Accepted Xth XXXXXXXXX 20XX

DOI: 10.1039/b000000x

Silver has been widely investigated as a cathode catalyst owing to its stable and high electrocatalytic activity in anion exchange membrane fuel cells (AEMFCs). In this work, we synthesize silver nanowires (Ag NWs) using polyol synthesis method and demonstrate that the supportless Ag NWs exhibit an extraordinarily high electrocatalytic activity toward the oxygen reduction reaction in a three-electrode cell. More significantly, the use of the supportless Ag NWs as the cathode catalyst in a H₂/O₂ AEMFC yields a peak power density of 164 mW cm⁻² at 60°C, which is favorably comparable to the state-of-the-art AEMFCs with carbon-supported Ag catalysts. In addition to the increased electrocatalytic activity, the improved performance is attributed to the elongated wire morphology of Ag NWs which allows a well-established porous electrode structure to form in the cathode. The high-performance supportless Ag NWs offer a promising alternative to carbon-supported electrocatalysts in fuel cells and metal-air batteries, to eliminate the carbon supporting materials.

1. Introduction

A resurgence of interest in anion exchange membrane fuel cells (AEMFCs) as low-temperature energy-conversion devices has been revitalized by the promising progress in alkaline anion exchange membranes (AAEMs).¹⁻⁴ The striking feature of AEMFCs is the significant improvements in the electrocatalytic activity and stability of catalysts in alkaline media. This merit allows the usage of non-precious catalysts for the oxygen reduction reaction (ORR) based on abundant transition metals. In this regard, silver owing to its stable and high electrocatalytic activity toward the ORR in alkaline media as well as the significant cost advantage over platinum and palladium, has been widely investigated as an ORR catalyst.⁵⁻⁷ Moreover, it is generally recognized that oxygen is reduced by Ag through a four-electron transfer pathway, which is a preferred pathway due to the higher currents available and the avoid of unwanted chemical intermediate produce (H₂O₂).

In addition to carbon-supported Ag nanoparticles (NPs)⁸, Ag nanocrystals with particular morphologies, such as nanocubes⁹, nanowires^{10, 11} and nanorods¹² have been synthesized and demonstrated to possess good electrocatalytic activities toward ORR, which is ascribed to the reduced oxygen/hydroxide absorption on the silver surface. Moreover, it has also been demonstrated that the activity of Ag-AEM interface is even higher than that of Ag with an aqueous alkaline solution.¹³ So far, only carbon-supported silver catalysts have been applied to fuel-cell systems but the performance has been reported to be relatively low.¹⁴⁻¹⁶ Other silver nanocatalysts, such as supportless

silver nanowires, however, have yet to be applied to a real fuel-cell system.

In this work, we synthesized supportless Ag nanowires (NWs) with a high aspect ratio and directly applied them to fabricate the cathode for H₂/O₂ AEMFCs. The electrocatalytic activity toward ORR was first evaluated in a conventional three-electrode cell. Due to their particular morphology, the supportless Ag NWs were then applied to fabricate the cathode for H₂/O₂ AEMFCs without other supporting materials. The performance of H₂/O₂ AEMFCs was tested with various Ag NWs loadings at different temperatures. The durability of H₂/O₂ AEMFCs was also investigated at a constant current discharge.

2. Experimental

2.1 Materials and Synthesis

Silver nitrate, ethylene glycol (EG) and poly (vinyl pyrrolidone) (PVP) were purchased from Sigma-Aldrich, all of which were of analytical grade. Deionized (DI) water with a resistivity of not less than 18.2 MΩ (Millipore) was prepared for all solutions. Ag NWs were synthesized based on a seed growth technique.^{10, 17} Generally, an EG solution (50 mL) containing 0.36 M PVP was refluxed in a three-necked flask at 170°C for 1 hour. The AgCl seeds were obtained through injection of 50 μL of EG solution of NaCl (0.1 M) and 60 μL of EG solution of AgNO₃ (0.05 M). After 30 minutes, 60 ml of EG solution of AgNO₃ (0.05 M) was added into the solution (about 2 mL min⁻¹). The reaction continued at 170°C for another 30 minutes, after which time the mixture was quenched in an ice bath. The free-

standing Ag NWs were collected by centrifugation and dispersed into acetone.

2.2 Physical characterization

Transmission electron microscopy (TEM) images were obtained by operating a high-resolution JEOL 2010F TEM system with a LaB₆ filament at 200 kV. The samples were dispersed in ethanol under sonication and dripped onto the holey carbon-coated Cu grids. The X-ray diffraction (XRD) patterns of the samples were analyzed with a Philips high resolution x-ray diffraction system (model PW 1825) using a Cu K α source operating at 40 keV with a scan rate of 0.025° s⁻¹. Surface morphology of Ag NWs were performed on a JEOL 6700F. The cross-section morphology of electrode structure was performed on a JEOL-6300F with SEM-EDX mapping operated at 15 kV.

2.3 Electrochemical characterization

All electrochemical measurements were carried out in a standard three-electrode cell using a RDE setup from Pine Instruments connected to a potentiostat (Autolab, PGSTAT30). A Pt foil and an Ag/AgCl (3.0 M KCl) were employed as the counter electrode and reference electrode, respectively. Typically, 2 mg Ag NWs and 20 μ L of a home-made ionomer (10wt.%)¹⁸ were dispersed in 2 mL of ethanol, followed by sonication for 1 hour to form a uniform ink. The catalyst ink was then dripped on a pre-polished glassy carbon electrode (5 mm diameter, Pine Instruments). Cyclic voltammogram was measured in a N₂-saturated 0.1 M KOH with a scan rate of 50 mV s⁻¹. ORR polarization curves were obtained in an O₂-saturated 0.1 M KOH by varying rotating speed from 400 rpm to 1600 rpm with the scan rate of 5 mV s⁻¹. Koutecky-Levich plots (j^{-1} vs. $\omega^{-1/2}$) were analyzed at various electrode potentials. The slopes of their best linear fit lines were used to calculate the electron transfer number (n) and kinetic current densities on the basis of the Koutecky-Levich equation:

$$\frac{1}{j} = \frac{1}{j_k} + \frac{1}{j_d} = \frac{1}{j_k} + \frac{1}{B\omega^{1/2}} \quad (1)$$

$$B = 0.2nF(D_{O_2})^{2/3}\nu^{-1/6}C_{O_2} \quad (2)$$

where j is the measured current density, j_k and j_d are the kinetic and diffusion-limiting current density, respectively. ω is the angular velocity (rpm), n is the transferred electron number, F is the Faraday constant, D_{O_2} is the diffusion coefficient of O₂ in 0.1 M KOH (1.86×10^{-5} cm² s⁻¹), ν is the kinematic viscosity (1.008×10^{-2} cm² s⁻¹), C_{O_2} is the bulk concentration of O₂ (1.21×10^{-6} mol cm⁻³).^{19, 20}

All potentials were reported versus reversible hydrogen electrode (RHE) unless otherwise stated. The potentials versus Ag/AgCl electrode was calibrated with respect to reversible hydrogen electrode (RHE) using the following equation:

$$E(\text{RHE}) = E(\text{Ag/AgCl}) + 0.197 + 0.0592 \times \text{pH}$$

2.4 Fuel cell performance

The fuel cell performance was measured in a hardware (Fuel Cell Technologies, Inc.) installed on an Arbin fuel cell testing system. Tokuyama A901 membrane was employed as the AEM (The thickness is 10 μ m; the ionic exchange capacity and ionic conductivity is 1.7 mmol g⁻¹ and 38 mS cm⁻¹ at 23°C, respectively).²¹ A catalyst ink consisted of Ag NWs and the

home-made ionomer were spray-coated on one side of A901 (Tokuyama), which was sprayed with a layer of interfacial ionomer with a loading of 1.0 mg_{ionomer} cm⁻² in advance. The catalyst loading was controlled by weighing with a microbalance. Pt/C catalysts (60 wt.% metal loading, Johnson Matthey Corp.) as the anode catalysts were spray-coated on the other side of A901 to form a catalyst-coated membrane (CCM). The Pt/C loading in the anode was controlled within 0.5 mg_{Pt} cm⁻². The ionomer loading on both anode and cathode was 20 wt.%. Membrane electrode assemblies (MEAs) were formed by sandwiching the CCM between the gas-diffusion layers (SIGRACET GDL 25BC). The single cell was operated at 60°C and H₂/O₂ humidifier temperatures were set 5°C higher than that of cell temperature. To avoid the condensation of vaporous water, the pipes in both anode gas inlet and cathode gas inlet were also heated with the same temperature of humidifier. Fully humidified hydrogen and oxygen with the same flow rate of 500 mL min⁻¹ were separately fed into the anode and cathode channel. The back pressure in anode and cathode was maintained at 30 psi during the measurement process. Humidification of the MEA was performed for 0.5 hour by flowing N₂ (100% RH) on both anode and cathode at a cell temperature of 60°C. MEAs were then activated by cycling between OCV and 100 mV with a decrement step of 100 mV every 5 minutes, until stable performance between two cycles was obtained. Polarization curves were collected by applying a current staircase with the duration of 3 minutes at each current. The durability of MEAs was carried out at a constant current discharge.

3. Results and Discussion

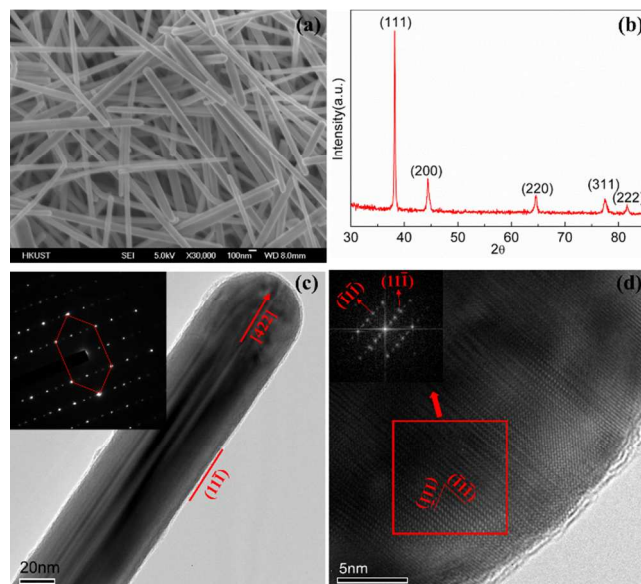


Fig. 1 A Typical SEM image (a) and XRD pattern of Ag NWs (b). A typical TEM image of Ag NWs (c) (inset: SAED pattern). (d) High-resolution TEM image of Ag NWs (inset: the corresponding FFT pattern).

A typical morphology of Ag NWs is shown in Fig. 1a and Fig. S1, from which it is observed that nanowires with the diameter in the range of 40-60 nm and the length of up to ~30 μ m are obtained using the polyol synthesis method. The content of multiple-twinned particles (MTPs) remaining in the as-

synthesized products is less than 5 wt.%. Furthermore, MTPs can be readily separated by using a centrifuge rotating at 2000 rpm. The XRD pattern of Ag NWs is shown in Fig. 1b. All the peaks can be indexed to the face centered cubic (*fcc*) silver crystal. The lattice constant calculated from this XRD pattern is 4.093 Å, which is close to the standard data ($a=4.086$ Å, JCPDS#04-0783). Fig. 1c shows a typical TEM image of a single silver nanowire, clearly indicating the existence of a twin-plane structure parallel to the crystal growth direction.²² The structure was further confirmed by corresponding selected area electron diffraction pattern (inset) which consists of two sets of spots, demonstrating the formation of a five-fold twinned structure. To determine the crystalline structure of Ag NWs, the high-resolution TEM (HRTEM) of silver nanowire is presented in Fig. 1d. The figure further reveals that Ag NWs possess a twin crystalline structure according to the fast Fourier transform (FFT) patterns (inset of Fig. 1d). It is also shown that Ag NWs are enclosed with the {111} planes acting as the surface planes with a corresponding growth direction of [422].^{22, 23}

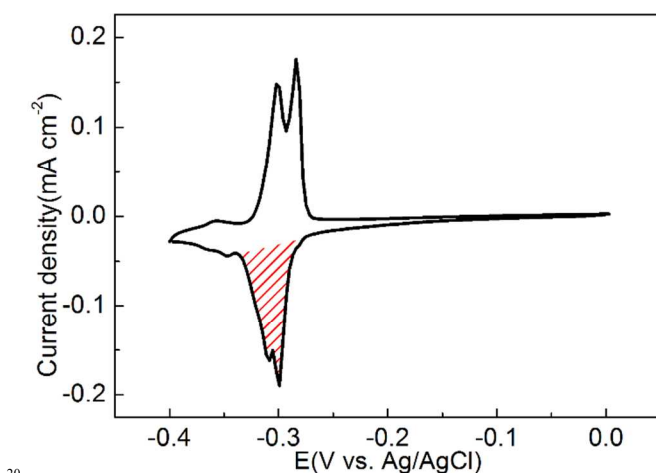


Fig. 2 CV curves of Pb UPD in Ag/rGO and Ag NWs catalyst

The electrochemical surface area (ECSA) was then evaluated through analyzing the charge associated with Pb underpotential deposition (UPD) on Ag NWs. The experiment was carried out in an electrolyte solution of 12 mM Pb(NO₃)₂+0.1 M KOH+10 mM NaClO₄ at a scan rate of 10 mV s⁻¹. Fig. 2 shows the cyclic voltammetry (CV) curve of Pb UPD on the as-prepared Ag NWs. The presence of reversible adsorption/desorption peak pairs in Ag NWs indicates a stepwise formation of the UPD Pb overlayer, probably arising from the wire-like morphology.^{24, 25} Assuming that the theoretical adsorption charge of a Pb monolayer on silver is 260 μC cm⁻², the corresponding ECSA is 5.14 m² g⁻¹, which is comparable with the result reported elsewhere.^{6, 17, 26}

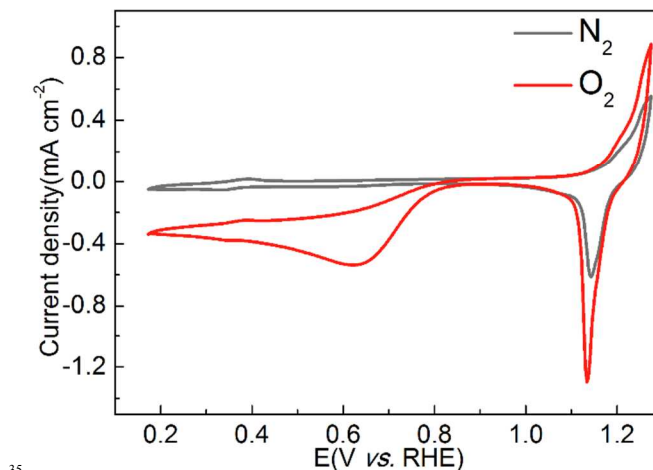


Fig. 3 CV curves of Ag NWs in N₂-saturated (gray lines) or O₂-saturated (red lines) 0.1 M KOH.

The electrocatalytic activity of Ag NWs was then characterized by CV in a N₂-saturated 0.1 M KOH. The peaks ranging from +1.1 V to +1.3 V are associated with the formation/dissolution of the AgOH monolayer. Noted that the formation of bulk phases of AgOH and Ag₂O will be appeared if the potential further scans to more anodic direction.^{23, 27} To avoid this formation, the cutoff potential at the positive side was set to +1.3 V. It can be measured the ECSA from Ag oxidation reaction according to the assumption that the theoretical adsorption charge of AgOH monolayer is 400 μC cm⁻².^{17, 28} Based on this evaluation, the ECSA of Ag NWs is 5.31 m² g⁻¹, which is consistent with the result calculated from Pb UPD. Meanwhile, the ORR activity can be observed from the apparent reduction peaks at about +0.65 V which emerged on the CV curve of the Ag NWs in O₂-saturated 0.1 M KOH when compared with the CV curve in N₂-saturated 0.1 M KOH. The ORR activity for Ag NWs were further examined by rotating disk electrode (RDE) voltammetry in an O₂-saturated 0.1 M KOH solution at a sweep rate of 5 mV s⁻¹. Fig. 4 shows the linear sweep voltammetry (LSV) curves at various rotation rates. It is revealed that Ag NWs exhibit a onset potential (0.1 mA cm⁻² in the RDE experiment²⁹) and a half-wave potential (E_{1/2}) at 1600 rpm are +0.92 V and +0.78 V, respectively. The onset potential and E_{1/2} are more positive than those of Ag/C catalyst reported elsewhere (+0.85 V and +0.56 V)⁶, indicating Ag NWs exhibit a high activity toward ORR. Meanwhile, the electron transfer number (*n*) and specific activity toward ORR were analysed by the Koutecky-Levich equation, as shown in Fig. S2. It can be seen that Ag NWs enable the reduction of O₂ to OH⁻ in alkaline media, predominantly through a 4e⁻ reduction process in the entire calculated potential range. The intrinsic kinetic current density at +0.9 V or +0.85 V is commonly considered as a benchmark to evaluate the specific activities of ORR catalysts.³⁰ Based on the ECSA calculated from Pb UPD, the specific activity for Ag NWs at +0.85V is 0.081 mA cm_{Ag}⁻², which is favorably comparable to the specific activity reported in the open literature.^{6, 17} The enhanced specific activity is ascribed to the presence of the {110} facet at the end plane of Ag NWs, which was demonstrated as the most active low-index Ag facet.^{17, 31} Meanwhile, Tafel slope changes from 58 mV/decade to 170 mV/decade when the overpotential increases (Fig. S2). The two segmentations with different slopes were

widely observed in the ORR process, indicating that the coverage conditions of the reaction intermediate was changed.³²

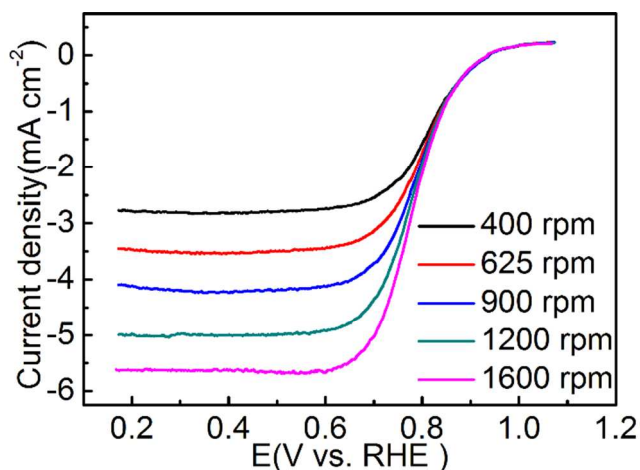


Fig. 4 LSV curves of Ag NWs in O₂-saturated 0.1 M KOH at various rotation rates with a sweep rate of 5 mV s⁻¹ at room temperature. All of the currents are normalized in reference to the geometrical surface area.

The durability of Ag NWs toward ORR was also measured with the DOE accelerated durability test protocol in N₂-saturated 0.1 M KOH.³³ The LSV curves before and after different cycling numbers with the rotating speed of 1600 rpm are presented in Fig. 5. The E_{1/2} is negatively shifted about 12 mV and 21 mV after 2,000 cycles and 4,000 cycles, respectively. It should be noted that there is no specific mechanism to explain the degradation of nanowire-like morphology for ORR currently. Due to the peculiar elongated wire morphology and the absence of the carbonaceous materials, the Ostwald ripening, aggregation and carbon corrosion should be eliminated. The degradation likely results in the partly Ag oxidation or the mild dissolution of Ag.³⁴⁻³⁶ In situ TEM observation is an effective technique to elucidate the detailed degradation mechanism and this part of work is in progress in our group.

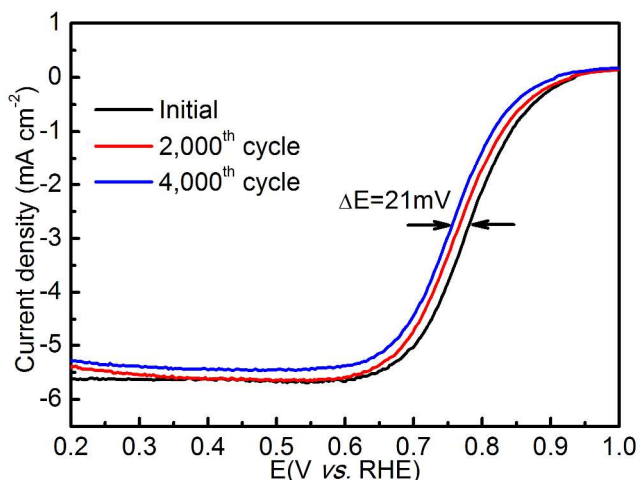


Fig. 5 LSV curves of Ag NWs before and after different cycling numbers in N₂-saturated 0.1 M KOH. The DOE accelerated durability test protocol was applied in the measurements.

The cell performance of MEA using supportless Ag NWs as the cathode catalyst was evaluated in a real fuel-cell system. The morphological structure and the cross section of the MEA

fabricated with supportless Ag NWs as the cathode were characterized by SEM-energy-dispersive-X-ray (EDX). As shown in Fig. 6a, it is seen that the established porous electrode structure is similar with that of the conventional electrode structure using the carbon-supported catalysts,³⁷ despite the fact that the porosity is different. The porosity of the anode and cathode are estimated in the supplementary information (44.16% for anode vs. 9.52% for cathode). The cross section of MEA is presented in Fig. 6b where the cathode is located at the top of the figure, anion exchange membrane in the middle, and the anode at the bottom (commercial Pt/C catalyst). The respective thicknesses for each layers are 4.2 μm, 11.6 μm and 7.7 μm. The catalyst layer and membrane are clearly distinguished, while an interface layer is sandwiched between them. The element distribution conducted by EDX mapping analysis is also shown in Fig. 6b where the Ag and Pt elements are derived from the cathode and anode, respectively. The nitrogen signal for membrane and ionomer is evenly overlapped across the entire sample, indicating a uniform distribution of the ionomer in the catalyst layer. Meanwhile, the catalyst layers are in intimate contact with interface layers, which will be beneficial to transporting hydroxide ions.

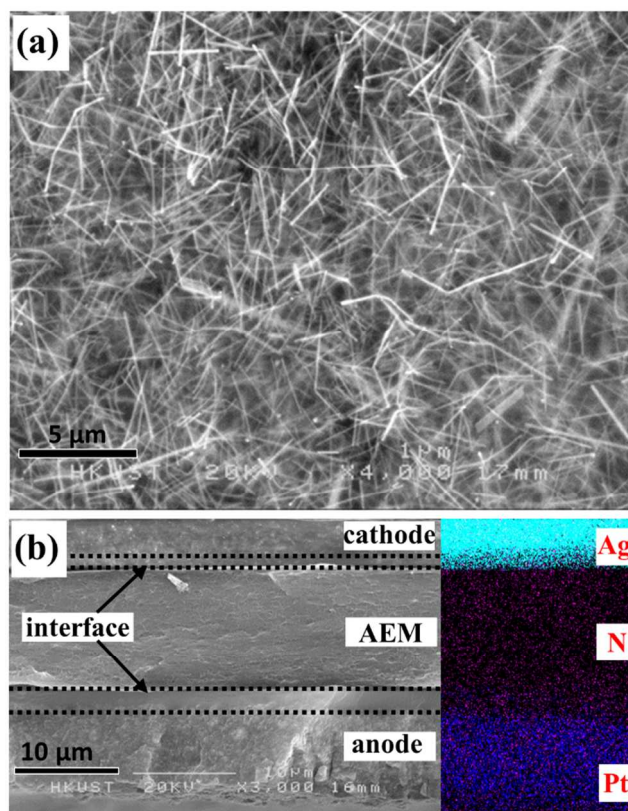


Fig. 6 (a) surface topography of the cathode using supportless Ag NWs; (b) cross-section of MEA with the element mapping. Ag NWs loading: 1.05 mg cm⁻²

Fig. 7a presents the polarization and power density curves with various Ag loading in the cathode. Due to the specific absorption of quaternary ammonium functional groups on the catalyst surface, a high ionomer loading in the catalyst layer will lead to a large coverage of electroactive sites, thereby reducing the active surface areas of catalyst.³⁸⁻⁴⁰ However, the open circuit voltage for all the MEAs employing Ag NWs is above 1.0 V,

implying that the ionomer does not affect the catalyst utilization significantly. An improvement in cell performance is observed with an increase in the Ag loading ranging from 0.25 mg cm^{-2} to 1.05 mg cm^{-2} . Beyond this loading, a decrease in cell performance is found. With high Ag loading in the electrode, a high concentration overpotential in the high current density region is also observed, which can be ascribed to the decrease in the cathode porosity resulting in a shrunken pathway for oxygen gas to diffuse. The high-frequency resistance measured with AC impedance are $2.63 \Omega \text{ cm}^2$, $1.69 \Omega \text{ cm}^2$, $1.04 \Omega \text{ cm}^2$ and $1.16 \Omega \text{ cm}^2$ when the Ag NWs loading in the cathode increases from 0.25 mg cm^{-2} to 1.05 mg cm^{-2} . It is known that Ag is good electrical conductor, hence the high resistance might be caused by the absorption of quaternary-based ionomer on the Ag surface.

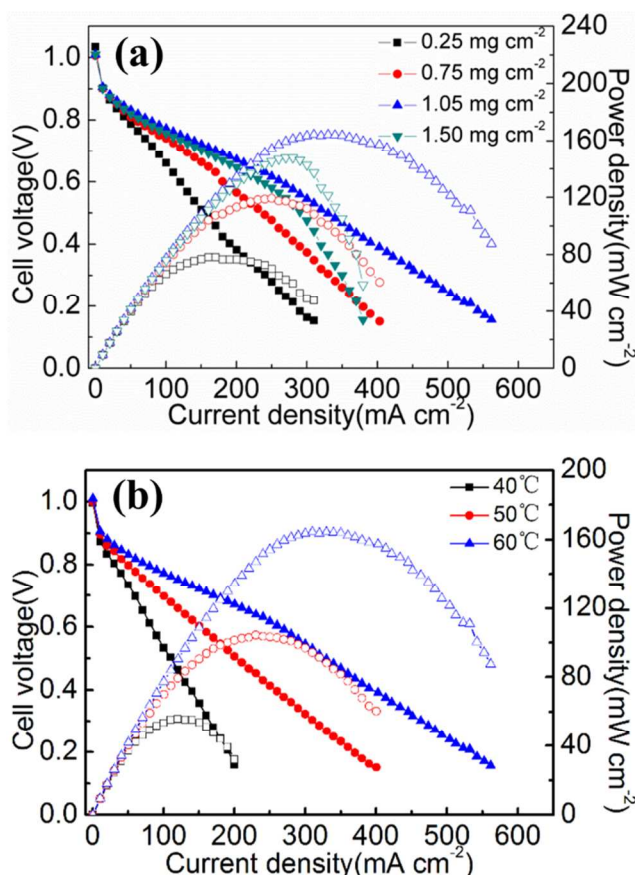


Fig. 7 (a) Polarization curves (filled symbols) and power density curves (empty symbols) of H_2/O_2 AEMFCs with various Ag loadings. Cell temperature: 60°C ; (b) Polarization curves (filled symbols) and power density curves (empty symbols) of H_2/O_2 AEMFCs at different temperatures. Anode: hydrated hydrogen gas, 500 sccm ; cathode: hydrated oxygen gas, 500 sccm .

Fig. 7b presents the polarization and power density curves of the fuel cell employing 1.05 mg cm^{-2} Ag NWs as the cathode at different temperatures. The increased temperature results in a decrease in membrane resistance and an enhancement in electrochemical kinetics of electrodes, both of which contribute to the cell performance improvement. However, the operating temperature did not further increase since the membrane suffers a severe degradation above 60°C . It is noteworthy that this is the first time supportless Ag NWs are employed as the cathode to achieve a power density of 164.4 mW cm^{-2} , which is favorably

comparable to the cell performance of AEMFCs employing carbon-supported Ag catalysts, as summarized in Table 1.

Table 1 Comparison of the AEMFC performance using Ag-based catalysts as the cathode

Catalyst (loading)	Membrane	Oxidants (BP)	Temperature	PPD	Ref.
Ag/C(0.5)	AHA(Neosepta) ^a	$\text{O}_2(0)$	30°C	10	41
Ag/C(0.5)	APSEBS ^b	$\text{O}_2(0)$	60°C	109	42
Ag/C(2.0)	TMHDA-QAPSF ^c	Air(0)	60°C	30.1	16
Ag/C(4.0)	TMHDA-QAPVBC ^d	$\text{O}_2(0)$	50°C	~48	43
Ag/C(1.0)	A201(Tokuyama) ^e	$\text{O}_2(30)$	80°C	190	44
Ag/C(2.0)	Unknown	$\text{O}_2(20)$	50°C	~270	45
Ag NWs(1.05)	A901(Tokuyama) ^e	$\text{O}_2(30)$	60°C	164.4	This work

loading: mg cm^{-2} ; BP: back pressure, psi; PPD: peak power density: mW cm^{-2} .

a) AHA membrane: tetra-alkyl ammonium groups bonded to a polyolefin backbone chain. b) alkalized poly(styrene ethylene butylene poly styrene). c) N,N,N',N' -tetramethyl-1,6-hexanediamine cross-linked quaternized polysulfone; d) N,N,N',N' -tetramethyl-1,6-hexanediamine cross-linked poly(vinylbenzyl chloride); e) A201 and A901 are the registered trademarks of Tokuyama.

To analyse the influence of supporting materials on the cell performance, graphene nanosheets (GNS, XFNano Material Tech Co., Ltd, lateral size: $0.5\text{--}5 \mu\text{m}$, surface area: $700 \text{ m}^2 \text{ g}^{-1}$) with the mass loading of 20 wt.% were added in the cathode catalyst layer. Here, the as-prepared Ag NWs were physically mixed with GNS (designated as Ag NWs + GNS), instead of deposited on GNS, to form the catalyst layer due to their high aspect ratio.²³ For a comprehensive comparison, the MEAs separately employing Ag/GNS (Fig. S3) and commercial Pt/C as the cathode catalyst were also prepared. The polarization curves and power density curves under otherwise identical fuel cell preparation and test conditions were measured, as illustrated in Fig. S4. When the cathode was fabricated with commercial Pt/C catalyst, the peak power density boosts to 364.5 mW cm^{-2} , which is comparable with the results reported in the literature.^{46, 47} It is also evident that the performance of MEA employing Ag NWs + GNS is indeed higher than that of MEA employing Ag NWs (e.g. peak power density: 194.5 mW cm^{-2} for Ag NWs + GNS vs. 164.3 mW cm^{-2} for Ag NWs; and maximum current density: 760 mA cm^{-2} for Ag + GNS vs. 560 mA cm^{-2} for Ag NWs). However, the enhanced performance is ascribed to the reduced mass-transport resistance in the high current density region, resulting from the electrode structure with larger porosity. Meanwhile, MEA employing Ag/GNS with the same Ag loading exhibits a peak power density of 287.8 mW cm^{-2} . The improvement in cell performance is attributed, in part, to the increase in the cathode porosity resulting in a smooth pathway for oxygen gas to diffuse, and in part, to the large ECSA ($10.65 \text{ m}^2 \text{ g}^{-1}$ for Ag/GNS vs. $5.14 \text{ m}^2 \text{ g}^{-1}$ for Ag NWs) for ORR (Fig. S5). However, the introduction of carbonaceous material inducing the carbon corrosion will cause the long-term stability issue, especially at evaluated temperature and high potential.

Further, the durability of MEA employing Ag NWs as the cathode with a loading of 1.05 mg cm^{-2} was investigated by

discharging at 200 mA cm^{-2} , as illustrated in Fig. 8. The MEA can continuously discharge for 100 hours when the cell voltage steady decrease from initial 0.605 V (1 hour) to 0.533 V (100 hour) with a voltage decay rate of 0.72 mV h^{-1} . Also, *in situ* AC impedance was performed before and after constant current discharge and the spectra are shown in Fig. S6. In the impedance spectra, the second semicircle with a larger time constant belongs to the cathode activation process due to the sluggish kinetics of ORR. It can be seen that the diameter of second semicircle becomes larger after long-term operation, which is ascribed to the degradation of cathode. The cathode decay might be caused by the following reasons: (1) the surface energy of Ag NWs drive Ag NWs to coalesce via crystal migration. (2) the change of porous nanostructure during the durability test, such as the accumulated water flooding, which makes the transport of gases more difficult. Due to the high aspect ratio of Ag NWs, the effect of Ag NW coalescence on performance degradation is likely insignificant.⁴⁸ Hence, the change of the porous nanostructure should be the main reason leading to the cathode degradation. Nevertheless, the stability of the MEA is acceptable with a relatively low degradation rate for the H_2/O_2 AEMFCs.

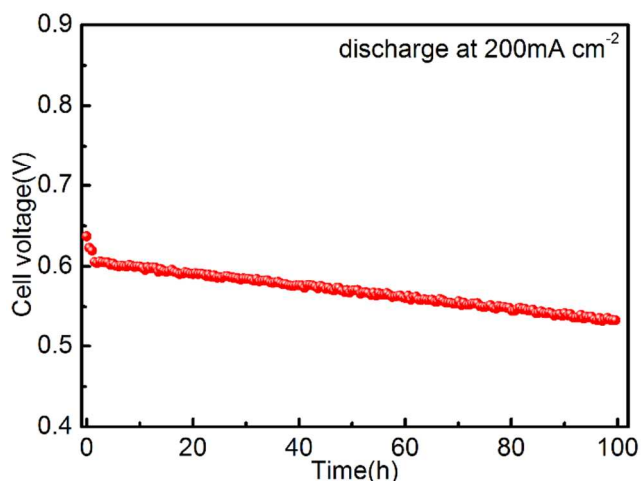


Fig. 8 Durability tests of AEMFCs at 60°C . Anode: hydrated hydrogen gas, 500 sccm; cathode: hydrated oxygen gas, 500 sccm.

4. Conclusions

In summary, we synthesized the supportless Ag NWs and applied them as the cathode catalyst in H_2/O_2 AEMFCs. The supportless Ag NWs with a high aspect ratio not only showed high electrocatalytic performance in the conventional three-electrode cell, but also enabled a H_2/O_2 AEMFC to yield a peak power density of 164 mW cm^{-2} at 60°C . The cell was also tested at a constant current density of 200 mA cm^{-2} for 100 hours, exhibiting a low degradation rate. We believe that the supportless Ag NWs can be employed as the high-activity ORR catalyst for not only fuel cells, but also metal-air batteries, to eliminate the carbon supporting materials.

Acknowledgements

The work described in this paper was fully supported by a grant from the Research Grants Council of the Hong Kong Special Administrative Region, China (Project No. HKUST9/CRF/11G).

Notes and references

Department of Mechanical and Aerospace Engineering, The Hong Kong University of Science and Technology, Clear Water Bay, Kowloon, Hong Kong SAR, China.

Fax: (852)23581543; Tel: (852) 23588647; E-mail: metzhao@ust.hk (T.S. Zhao)

† Electronic Supplementary Information (ESI) available: [details of any supplementary information available should be included here]. See DOI: 10.1039/b000000x/

- Y. J. Wang, J. L. Qiao, R. Baker and J. J. Zhang, *Chemical Society Reviews*, 2013, 42, 5768-5787.
- E. H. Yu, X. Wang, U. Krewer, L. Li and K. Scott, *Energ Environ Sci*, 2012, 5, 5668-5680.
- G. Couture, A. Alaaeddine, F. Boschet and B. Ameduri, *Prog Polym Sci*, 2011, 36, 1521-1557.
- H. W. Zhang and P. K. Shen, *Chem Rev*, 2012, 112, 2780-2832.
- B. B. Blizanac, P. N. Ross and N. M. Markovic, *J Phys Chem B*, 2006, 110, 4735-4741.
- E. J. Lim, S. M. Choi, M. H. Seo, Y. Kim, S. Lee and W. B. Kim, *Electrochem Commun*, 2013, 28, 100-103.
- M. A. Kostowskyj, R. J. Gilliam, D. W. Kirk and S. J. Thorpe, *Int J Hydrogen Energ*, 2008, 33, 5773-5778.
- N. Sharifi, F. Tajabadi and N. Taghavinia, *Int J Hydrogen Energ*, 2010, 35, 3258-3262.
- C. L. Lee, Y. L. Tsai, C. H. Huang and K. L. Huang, *Electrochem Commun*, 2013, 29, 37-40.
- K. Ni, L. Chen and G. X. Lu, *Electrochem Commun*, 2008, 10, 1027-1030.
- M. A. Kostowskyj, D. W. Kirk and S. J. Thorpe, *Int J Hydrogen Energ*, 2010, 35, 5666-5672.
- Y. Lu, Y. Wang and W. Chen, *J Power Sources*, 2011, 196, 3033-3038.
- A. E. S. Sleightholme, J. R. Varcoe and A. R. Kucernak, *Electrochem Commun*, 2008, 10, 151-155.
- S. Gu, W. C. Sheng, R. Cai, S. M. Alia, S. Q. Song, K. O. Jensen and Y. S. Yan, *Chem Commun*, 2013, 49, 131-133.
- J. R. Varcoe, R. C. T. Slade, G. L. Wright and Y. L. Chen, *J Phys Chem B*, 2006, 110, 21041-21049.
- J. S. Park, S. H. Park, S. D. Yim, Y. G. Yoon, W. Y. Lee and C. S. Kim, *J Power Sources*, 2008, 178, 620-626.
- S. M. Alia, K. Duong, T. Liu, K. Jensen and Y. S. Yan, *Chemsuschem*, 2012, 5, 1619-1624.
- L. Zeng and T. S. Zhao, *Electrochem Commun*, 2013, 34, 278-281.
- N. M. Markovic, H. A. Gasteiger and N. Philip, *J Phys Chem-US*, 1996, 100, 6715-6721.
- S. Y. Wang, D. S. Yu, L. M. Dai, D. W. Chang and J. B. Baek, *Acc Nano*, 2011, 5, 6202-6209.
- H. Yanagi and K. Fukuta, *Ecs Transactions*, 2008, 16, 257-262.
- Y. G. Sun and Y. N. Xia, *Adv Mater*, 2002, 14, 833-837.
- H. Y. Qin, L. B. Jiang, Y. C. He, J. B. Liu, K. Cao, J. Wang, Y. He, H. L. Ni, H. Z. Chi and Z. G. Ji, *J Mater Chem A*, 2013, 1, 15323-15328.
- U. Schmidt, S. Vinzelberg and G. Staikov, *Surf Sci*, 1996, 348, 261-279.
- J. Sackmann, A. Bunk, R. T. Potzschke, G. Staikov and W. J. Lorenz, *Electrochimica acta*, 1998, 43, 2863-2873.

26. E. Kirowa-Eisner, Y. Bonfil, D. Tzur and E. Gileadi, *J Electroanal Chem*, 2003, 552, 171-183.
27. J. S. Guo, A. Hsu, D. Chu and R. R. Chen, *J Phys Chem C*, 2010, 114, 4324-4330.
- 5 28. J. G. Becerra, R. Salvarezza and A. J. Arvia, *Electrochimica acta*, 1990, 35, 595-604.
29. G. Wu, K. L. More, C. M. Johnston and P. Zelenay, *Science*, 2011, 332, 443-447.
30. H. A. Gasteiger, S. S. Kocha, B. Sompalli and F. T. Wagner, *Appl Catal B-Environ*, 2005, 56, 9-35.
- 10 31. Y. G. Sun, B. Mayers, T. Herricks and Y. N. Xia, *Nano Lett*, 2003, 3, 955-960.
32. N. M. Markovic, H. A. Gasteiger and P. N. Ross, *J Phys Chem-Us*, 1995, 99, 3411-3415.
- 15 33. Y. G. Li, W. Zhou, H. L. Wang, L. M. Xie, Y. Y. Liang, F. Wei, J. C. Idrobo, S. J. Pennycook and H. J. Dai, *Nat Nanotechnol*, 2012, 7, 394-400.
34. J. C. Meier, C. Galeano, I. Katsounaros, A. A. Topalov, A. Kostka, F. Schuth and K. J. J. Mayrhofer, *Acs Catal*, 2012, 2, 832-843.
- 20 35. Z. W. Chen, M. Waje, W. Z. Li and Y. S. Yan, *Angew Chem Int Edit*, 2007, 46, 4060-4063.
36. Y. Z. Lu, Y. Y. Jiang and W. Chen, *Nano Energy*, 2013, 2, 836-844.
37. Y. C. Cao, X. Wang, M. Mamlouk and K. Scott, *J Mater Chem*, 2011, 21, 12910-12916.
- 25 38. M. Unlu, D. Abbott, N. Ramaswamy, X. M. Ren, S. Mukerjee and P. A. Kohl, *J Electrochem Soc*, 2011, 158, B1423-B1431.
39. M. Carmo, G. Doubek, R. C. Sekol, M. Linardi and A. D. Taylor, *J Power Sources*, 2013, 230, 169-175.
40. S. Gu, R. Cai, T. Luo, Z. W. Chen, M. W. Sun, Y. Liu, G. H. He and Y. S. Yan, *Angew Chem Int Edit*, 2009, 48, 6499-6502.
- 30 41. S. Maheswari, P. Sridhar and S. Pitchumani, *Electrocatalysis-Us*, 2012, 3, 13-21.
42. R. Vinodh and D. Sangeetha, *J Mater Sci*, 2012, 47, 852-859.
43. J. R. Varcoe, R. C. Slade, G. L. Wright and Y. Chen, *The Journal of Physical Chemistry B*, 2006, 110, 21041-21049.
- 35 44. Z. Z. Le Xin, Z. Wang, J. Qi and W. Li, *Frontiers in chemistry*, 2013, 1.
45. R. Chen, J. Guo, H. He, J. Zhou and D. Chu, 2012.
46. K. Fukuta, H. Inoue, Y. Chikashige and H. Yanagi, *Batteries and Energy Technology (General) - 217th Ecs Meeting*, 2010, 28, 221-225.
- 40 47. D. L. Yang, H. M. Yu, G. F. Li, Y. Zhao, Y. X. Liu, C. K. Zhang, W. Song and Z. G. Shao, *J Power Sources*, 2014, 267, 39-47.
48. W. Z. Li and P. Haldar, *Electrochem Commun*, 2009, 11, 1195-1198.
- 45